Sensors and Materials, Vol. 37, No. 4 (2025) 1681–1709
MYU Tokyo

S & M 4012

Optimization of Thermal Control Parameters for Laptop Computer Cooling System Using Finite Volume Method

Kuang-Chung Chen,[1] Min-Chie Chiu,[2*] Yu-HsinWang,[2]
Shih-Ming Cho,[3] and Tian-Syung Lan[4]

[1]School of Computer Science, Weifang University of Science and Technology,
No. 1299 Jinguang Street, Shouguang City 262700, Shandong Province, China
[2]Department of Mechanical and Materials Engineering, Tatung University,
No. 40, Sec. 3, Zhongshan N. Rd., Taipei City 10452, Taiwan
[3]Department of Computer Science and Engineering, Tatung University,
No. 40, Sec. 3, Zhongshan N. Rd., Taipei City 10452, Taiwan
[4]Department of Information Management, Yu Da University of Science and Technology,
Miaoli County 361, Zaoqiao Township, Taiwan

(Received November 11, 2024; accepted April 14, 2025)

Keywords: AI, CFD, cooling, finite volume method, microcontroller, laptop, optimization, temperature control

With the advent of AI technology, cloud computing power has been enhanced in edge computing used in personal devices such as laptop computers. To meet the computational demands, the performance of laptop computers has been improved. However, the improved performance leads to the heat generation of the central processing unit (CPU) and graphical processing unit (GPU). The limited size of the laptop computer limits the efficiency of its cooling system, which affects its stability and lifespan. Therefore, it is necessary to develop an optimized cooling system for the laptop computer using highly thermally conductive materials for efficient heat transfer. The cooling area and fan speed must be increased, and the air duct needs to be designed to increase airflow rate. Fan type and speed must be selected considering cooling effects. Appropriate heat pipes and radiators are also necessary to dissipate heat to the outside of the laptop computer. In this study, we developed an optimal cooling solution to improve the cooling efficiency of a laptop computer and compared it with existing ones. We adopted the finite volume method for the simulation, verification, and optimization of the developed solution. At ambient temperatures of 25, 30, and 35 °C, the fan speed was adjusted to 2800, 3200, and 4000 RPM to maintain the temperature of the CPU at 67.4, 67.3, and 67.1 °C, respectively.

*Corresponding author: e-mail: mcchiu@gm.ttu.edu.tw
https://doi.org/10.18494/SAM5463

ISSN 0914-4935
https://myukk.org/

1. Introduction

Laptop computers are essential in modern life as they are light and portable, making them appropriate for various purposes. However, laptop computers generate a large amount of heat when in use.[1] If such heat is not effectively dissipated to the outside, the central processing unit (CPU) and graphical processing unit (GPU) can become overheated, decreasing the performance and lifespan of the laptop computer and causing the system to be unstable. To dissipate the heat, fans are used at high speeds, generating significant noise[2] and negatively affecting the user experience.[3]

Amid the rapid development of AI technology, the cooling of AI computing systems has become increasingly important. High-performance AI hardware with high-performance CPUs, GPUs, and tensor processing units (TPUs) consumes a large amount of electrical power for deep learning and big data processing, resulting in significant heat generation.[4] If this heat is not effectively dissipated, the system performance may degrade, potentially causing damage. Therefore, an appropriate cooling system is critical in AI computing systems. The design of the cooling system of laptop computers is also crucial to increase their performance. One simple way to achieve efficient heat dissipation is by increasing the cooling area of electronic and mechanical components. This helps to transfer heat more effectively from the source to the outside.

In designing a cooling system, heat sinks, heat pipes, the topology optimization of radiators, and cooling materials must be chosen considering the overall cooling performance.[5] Heat sinks are widely used in electronic devices to dissipate the heat generated by the components of computers. In mechanical equipment, heat sinks disperse the heat of the internal combustion engine and the hydraulic system. Heat sinks are also utilized in cooling equipment such as air conditioners and refrigerators. In the design of heat sinks, their surface areas and volumes are used as indicators to measure their performance[6–9] as a larger surface area shows a stronger cooling effect.

Heat dissipation resistance is a measure of how the transfer of heat is impeded in a heat sink. The lower the heat dissipation resistance, the stronger the cooling effect. Heat dissipation efficiency is measured to estimate the effectiveness of a heat sink in transferring heat to the outside. The higher the efficiency, the stronger the cooling capability. Heat pipes are effective cooling components that are used to transfer heat from heat sources such as CPUs or GPUs to fans or heat sinks. Therefore, the design of heat pipes is crucial for laptop computers.[10] In laptop computers, heat pipes must be small but with reliable heat dissipation capability.

Cooling capacity is measured in watts (W). Mochizuki *et al.* and Wang *et al.* applied heat pipes in laptop computers and estimated their cooling efficiency.[11,12] Adham *et al.* analyzed the heat transfer and fluid dynamics of microchannel heat sinks in electronic devices.[13] To improve heat transfer, the topology of heat pipes must be optimized by establishing a mathematical model, defining design objectives, and setting design constraints.[14] For optimization, the mathematical model is constructed considering geometry, materials, thermal flow, and fluid dynamics. The purpose of the heat pipe design is to minimize the thermal or airflow resistance and constraints such as volume or weight. Rahman *et al.* discussed the effects of the thermal properties of the envelopes on the reduction in cooling load.[15] Their study focuses on multi-

objective optimization. The selection of the proper material is crucial for heat transfer in a cooling system.[16] The common materials used for the cooling system of a laptop computer are copper and aluminum owing to their high thermal conductivity, lightweight, and low cost. Graphite is also utilized because of its excellent thermal performance, although it is expensive.[17] Phase change materials (PCMs) are also often used as they absorb or release significant amounts of heat and effectively transfer heat.[18]

Various designs have been proposed to improve the cooling efficiency of laptop computers.[19,20] The positions, sizes, materials (cooling liquid and thermal paste), and numbers of cooling fans and air ducts have been explored.[19–22] To optimize the cooling effects, heat transfer in heat sinks is simulated to estimate their efficiency.[23] Wu *et al.* and Ghosh *et al.* improved the structural topology design to optimize heat conduction and cooling performance.[24,25] Ismail also used 3D modelling and the standard k-ω turbulent model to test the heat sink designs.[26] Deaton and Grandhi presented various cases of structural and continuous topology optimization while determining the thermal resistance.[27] Dilgen *et al.* based their topology cooling optimization for turbulent heat transfer, noting that flow resistance affects cooling efficiency.[28] Yuan and Coskun focused on finding materials with higher thermal conductivity, as increased data center and server performance has made heat dissipation one of the key considerations in server design.[29] The effect of the fan speed of a laptop computer on thermal management was also explored.[30–32] The cooling efficiency of laptop computers depends on the fan speed and ambient temperature. However, the impact of ambient temperature on the heat generation and transfer of the CPU in laptop computers has not yet been investigated. Thus, we explored the relationship and the combined effects of fan speed and ambient temperature on the cooling efficiency of the laptop computer in this study.

We combined the topology of air ducts (fan and air inlet), air inlets (inlet diameter and spacing), and heat sinks (length, width, and fin spacing), and static pressure and optimized parameters with forced convection. We analyzed the temperature of the CPU at different fan speeds and ambient temperatures and their relationship to maintaining a constant CPU temperature. A control system for the fan speed was developed to maintain a stable CPU temperature in accordance with the ambient temperature. The results provide the basis of the design of the cooling system of the laptop computer to maximize its cooling effect.

2. Mathematical Theories

We used the computational fluid dynamics (CFD) software for the thermal analysis of the laptop computer. Heat transfer and CFD equations were applied to analyze the pressure, velocity, and temperature.

2.1 Thermal transfer equations

2.1.1 Heat conduction

Thermal analysis equations involve multiple physical concepts, including heat conduction, convection, and radiation. The transfer of heat is simulated using Fourier's law of heat conduction

and the laws of heat convection and radiation. The CFD equations are used with Fourier's law of heat conduction in the finite volume method (FVM).

$$q = -k\nabla T, \tag{1}$$

where k is the thermal conduction coefficient of the material.

The heat conduction equation describes the process of heat transfer in solid materials. Depending on the dimensions of the analyzed object, the equation is expressed in one-, two-, and three-dimensional forms. We used the three-dimensional heat conduction equation as follows.

The one-dimensional heat conduction equation is applied to simplify heat conduction problems.

$$\frac{\partial T}{\partial t} = \alpha \frac{\partial^2 T}{\partial x^2} \tag{2}$$

The two-dimensional heat conduction equation is applied to heat conduction problems in two-dimensional structures such as planes or cylinders.

$$\frac{\partial T}{\partial t} = \alpha \left(\frac{\partial^2 T}{\partial x^2} + \frac{\partial^2 T}{\partial y^2} \right) \tag{3}$$

The three-dimensional heat conduction equation is applied to heat conduction problems in three-dimensional structures.

$$\frac{\partial T}{\partial t} = \alpha \left(\frac{\partial^2 T}{\partial x^2} + \frac{\partial^2 T}{\partial y^2} + \frac{\partial^2 T}{\partial z^2} \right) \tag{4}$$

2.1.2 Heat convection

In CFD, different forms of convection equations can be used to analyze electronic thermal problems under different fluid flow conditions. The heat convection equation describes the process of heat transfer in the laminar and turbulent flows. The law of heat convection describes the convective heat transfer as follows.

$$q = h\Delta T \tag{5}$$

The laminar convection equation is applied to slow fluid flows.

$$\frac{\partial T}{\partial t} + u\frac{\partial T}{\partial x} + v\frac{\partial T}{\partial y} + w\frac{\partial T}{\partial z} = \alpha \nabla^2 T \tag{6}$$

The turbulent convection equation is applied to very slow fluid flows.

$$\frac{\partial T}{\partial t}+\left(u\frac{\partial T}{\partial x}+v\frac{\partial T}{\partial y}+w\frac{\partial T}{\partial z}\right)+\frac{\partial\left(\rho k_t\frac{\partial T}{\partial x}\right)}{\partial x}+\frac{\partial\left(\rho k_t\frac{\partial T}{\partial y}\right)}{\partial y}+\frac{\partial\left(\rho k_t\frac{\partial T}{\partial z}\right)}{\partial z} = \rho c_p\left(\frac{\partial(uT)}{\partial x}+\frac{\partial(vT)}{\partial y}+\frac{\partial(wT)}{\partial z}\right) \tag{7}$$

Here, k_t is the turbulent heat conductivity.

2.1.3 Heat radiation

The radiation equation describes the process of heat transfer in electromagnetic waves with grey or nongrey radiation. For grey radiation, the emissivity of the material is assumed to be constant across different wavelengths [Eq. (8)] in contrast to nongrey radiation [Eq. (9)].

$$\sigma\varepsilon T^4-\dot{q}_{in}=\rho\varepsilon T_{ref}^4 \tag{8}$$

$$\int\left[\rho\varepsilon(\lambda)T^4-\dot{q}_{in}(\lambda)\right]d\lambda=0 \tag{9}$$

Here, $\varepsilon(\lambda)$ is the emissivity of the material at wavelength λ. In CFD, different forms of radiation equations are used to analyze the heat dissipation of different materials.

In addition to the above equations, the solid–liquid phase change, contact resistance, and natural convection are considered in the heat dissipation process of electronic components. The solid–liquid phase change and contact resistance at the interface between different materials hinder heat transfer, while natural convection, in the absence of forced convection, affects heat conduction. In this study, CFD was used to simulate heat dissipation by incorporating such factors.

2.2 CFD equations

CFD is commonly used to simulate fluid flow and heat transfer when using fans to obtain the parameters of fan flow. In CFD, Navier–Stokes, continuity, and energy conservation equations are used frequently.

2.2.1 Heat conduction

A change in velocity on the y-axis within an element of small-volume fluid is depicted in Fig. 1, assuming that the volume and the mass charge rate to time are not changed [Eq. (10)].

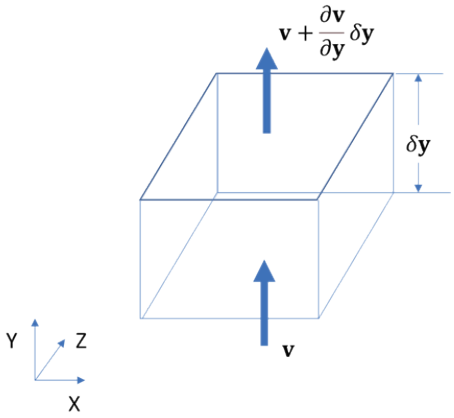

Fig. 1. (Color online) Velocity on y-axis in small-volume fluid element with δx, δy, and δz.

$$\dot{M} = \frac{\partial \rho}{\partial t}\delta x \delta y \delta z \tag{10}$$

The flow out ($flow_{out}$) of the volume is expressed as follows.

$$\left(\rho u + \frac{\partial \rho u}{\partial x}\delta x\right)\delta y \delta z \tag{11}$$

$$Net_{flow\text{-}out} = -(flow_{out} - flow_{in}) \tag{12}$$

$$Net_{flow-out} = -\frac{\partial \rho u}{\partial x}\delta x \delta y \delta z \tag{13}$$

In three dimensions,

$$Net_{flow-out} = \left(\frac{\partial \rho u}{\partial x} + \frac{\partial \rho v}{\partial y} + \frac{\partial \rho w}{\partial z}\right)\delta x \delta y \delta z. \tag{14}$$

The sum of the mass change rate ($\dot{M}$) and the net flow of mass out ($Net_{flow\text{-}out}$) equals zero.

$$\frac{\partial \rho}{\partial t}\delta x \delta y \delta z + \left(\frac{\partial \rho u}{\partial x} + \frac{\partial \rho v}{\partial y} + \frac{\partial \rho w}{\partial z}\right)\delta x \delta y \delta z = 0 \tag{15}$$

For an infinitely small volume (*i.e.*, $\delta x \delta y \delta z \to 0$), it yields

$$\frac{\partial \rho}{\partial t} + \left(\frac{\partial \rho u}{\partial x} + \frac{\partial \rho v}{\partial y} + \frac{\partial \rho w}{\partial z}\right) = 0. \tag{16}$$

2.2.2 Momentum equation

A change in normal stress σ_y is demonstrated in Fig. 2. A change in shear stress τ_{xz} on the y-axis is presented in Fig. 3.

The net normal stresses σ_x, σ_y, and σ_z in the x-, y-, and z-directions are expressed as $\frac{\partial \sigma_x}{\partial x}\delta x\delta y\delta z$, $\frac{\partial \sigma_y}{\partial y}\delta x\delta y\delta z$, and $\frac{\partial \sigma_z}{\partial z}\delta x\delta y\delta z$, respectively. The net shear stresses in the x-, y-, and z-directions are described as $\left(\frac{\partial \tau_{xy}}{\partial y}+\frac{\partial \tau_{xz}}{\partial z}\right)\delta x\delta y\delta z$, $\left(\frac{\partial \tau_{yx}}{\partial z}+\frac{\partial \tau_{yz}}{\partial x}\right)$, and $\left(\frac{\partial \tau_{zx}}{\partial y}+\frac{\partial \tau_{zy}}{\partial x}\right)$, respectively.

The change in velocity $\vec{\boldsymbol{U}}$ is given as

$$\delta\vec{\boldsymbol{U}}=\left(\frac{\partial\vec{\boldsymbol{U}}}{\partial \boldsymbol{x}}\delta \boldsymbol{x}+\frac{\partial\vec{\boldsymbol{U}}}{\partial \boldsymbol{y}}\delta \boldsymbol{y}+\frac{\partial\vec{\boldsymbol{U}}}{\partial \boldsymbol{z}}\delta \boldsymbol{z}\right)+\frac{\partial\vec{\boldsymbol{U}}}{\partial \boldsymbol{t}}\delta \boldsymbol{t}, \tag{17}$$

where δU is the sum of U change in volume and U change in time.

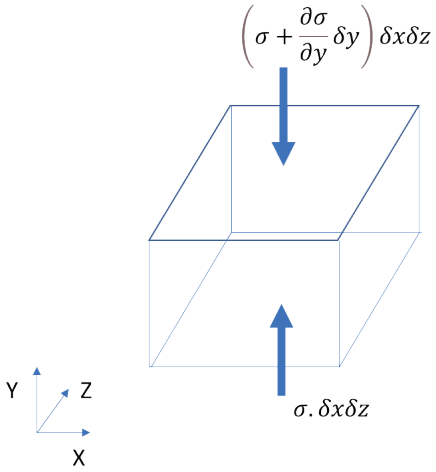

Fig. 2. (Color online) Change in normal stress σ_y in small-volume fluid element.

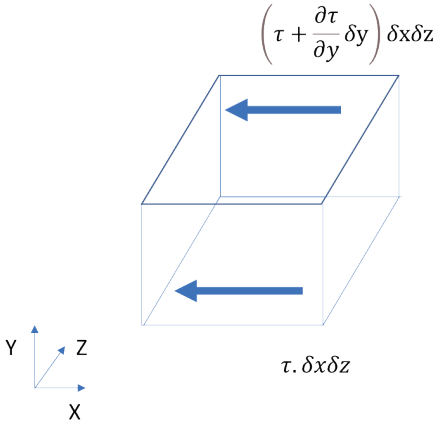

Fig. 3. (Color online) Change in shear stress τ_{xz} on y-axis in small-volume fluid element.

Dividing Eq. (16) by δt yields

$$\frac{\delta \vec{\boldsymbol{U}}}{\delta \boldsymbol{t}} = \left(\frac{\partial \vec{\boldsymbol{U}}}{\partial \boldsymbol{x}} \frac{\delta \boldsymbol{x}}{\delta \boldsymbol{t}} + \frac{\partial \vec{\boldsymbol{U}}}{\partial \boldsymbol{y}} \frac{\delta \boldsymbol{y}}{\delta \boldsymbol{t}} + \frac{\partial \vec{\boldsymbol{U}}}{\partial \boldsymbol{z}} \frac{\delta \boldsymbol{z}}{\delta \boldsymbol{t}} \right) + \frac{\partial \vec{\boldsymbol{U}}}{\partial \boldsymbol{t}}. \tag{18}$$

The mass of the fluid element is $\rho\delta x\delta y\delta z$. Considering the body $\boldsymbol{F}\left(= f_x\vec{i} + f_y\vec{j} + f_z\vec{k}\right)$ and plugging net normal and shear stresses, Eq. (18), as Newton's 2nd Law, yields

$$\rho\left(\frac{\partial u}{\partial x}u + \frac{\partial u}{\partial y}v + \frac{\partial u}{\partial z}\ w + \frac{\partial u}{\partial t} \right) = \left(\frac{\partial \sigma_x}{\partial x} + \frac{\partial \tau_{xy}}{\partial y} + \frac{\partial \tau_{xz}}{\partial z} \right) + f_x, \tag{19a}$$

$$\rho\left(\frac{\partial v}{\partial x}u + \frac{\partial v}{\partial y}v + \frac{\partial v}{\partial z}w + \frac{\partial v}{\partial t} \right) = \left(\frac{\partial \sigma_y}{\partial y} + \frac{\partial \tau_y x}{\partial x} + \frac{\partial \tau_y z}{\partial z} \right) + f_y, \tag{19b}$$

$$\rho\left(\frac{\partial w}{\partial x}u + \frac{\partial w}{\partial y}v + \frac{\partial w}{\partial z}w + \frac{\partial w}{\partial t} \right) = \left(\frac{\partial \sigma_z}{\partial z} + \frac{\partial \tau_{zx}}{\partial x} + \frac{\partial \tau_{xy}}{\partial y} \right) + f_z. \tag{19c}$$

In a Newtonian fluid, the normal and shear stresses related to the fluid pressure and viscosity are expressed as follows.

$$\sigma_x = -p + 2\mu\frac{\partial u}{\partial x} \tag{20a}$$

$$\sigma_y = -p + 2\mu\frac{\partial v}{\partial y} \tag{20b}$$

$$\sigma_z = -p + 2\mu\frac{\partial w}{\partial z} \tag{20c}$$

$$\tau_{xy} = \mu\left(\frac{\partial \boldsymbol{u}}{\partial \boldsymbol{y}} + \frac{\partial \boldsymbol{v}}{\partial \boldsymbol{x}} \right) \tag{20d}$$

$$\tau_{xz} = \mu\left(\frac{\partial \boldsymbol{u}}{\partial \boldsymbol{z}} + \frac{\partial \boldsymbol{w}}{\partial \boldsymbol{x}} \right) \tag{20e}$$

$$\tau_{yz} = \mu\left(\frac{\partial \boldsymbol{w}}{\partial \boldsymbol{y}} + \frac{\partial \boldsymbol{v}}{\partial \boldsymbol{z}} \right) \tag{20f}$$

Substituting Eqs. (20) into Eq. (19) yields the Navier–Stokes equation:

$$\rho\left(\frac{\partial u}{\partial x}u+\frac{\partial u}{\partial y}v+\frac{\partial u}{\partial z}w+\frac{\partial u}{\partial t}\right)=\frac{\partial}{\partial x}\left(-p+2\mu\frac{\partial u}{\partial x}\right)+\frac{\partial}{\partial y}\left[\mu\left(\frac{\partial v}{\partial x}+\frac{\partial u}{\partial y}\right)\right]+\frac{\partial}{\partial z}\left[\mu\left(\frac{\partial w}{\partial x}+\frac{\partial u}{\partial z}\right)\right]+f_x, \quad (21a)$$

$$\rho\left(\frac{\partial v}{\partial x}u+\frac{\partial v}{\partial y}v+\frac{\partial v}{\partial z}w+\frac{\partial v}{\partial t}\right)=\frac{\partial}{\partial x}\left(-p+2\mu\frac{\partial v}{\partial x}\right)+\frac{\partial}{\partial y}\left[\mu\left(\frac{\partial v}{\partial x}+\frac{\partial v}{\partial y}\right)\right]+\frac{\partial}{\partial z}\left[\mu\left(\frac{\partial w}{\partial x}+\frac{\partial v}{\partial z}\right)\right]+f_y, \quad (21b)$$

$$\rho\left(\frac{\partial w}{\partial x}u+\frac{\partial w}{\partial y}v+\frac{\partial w}{\partial z}w+\frac{\partial w}{\partial t}\right)=\frac{\partial}{\partial x}\left(-p+2\mu\frac{\partial w}{\partial x}\right)+\frac{\partial}{\partial y}\left[\mu\left(\frac{\partial w}{\partial x}+\frac{\partial w}{\partial y}\right)\right]+\frac{\partial}{\partial z}\left[\mu\left(\frac{\partial w}{\partial x}+\frac{\partial w}{\partial z}\right)\right]+f_z. \quad (21c)$$

A vector form of the Navier–Stokes equation is expressed as

$$\rho\left[\frac{\partial\vec{\boldsymbol{U}}}{\partial t}+\left(\vec{\boldsymbol{U}}\cdot\nabla\right)\vec{\boldsymbol{U}}\right]=-\nabla\vec{\boldsymbol{P}}+\mu\nabla^2\vec{\boldsymbol{U}}+\rho\vec{g}. \quad (22)$$

In the analysis of fluid dynamics and thermal transfer, the gravity acting in the *y*-direction is considered.

$$f_y=\frac{1}{p}g\left(p_{ref}-\rho\right)\delta x\delta y\delta z \quad (23)$$

Considering the buoyancy force in the *y*-direction, the Boussinesq approximation is formatted as follows.[33]

$$f_y=g\beta\left(T-T_{ref}\right)\delta x\delta y\delta z \quad (24a)$$

$$\text{where } \beta=-\frac{1}{p}\left(\frac{\partial\rho}{\partial T}\right)_{\boldsymbol{p}} \quad (24b)$$

The performance parameters for airflow were obtained using CFD. In a steady flow, we ignored the changes in air density and the effect of buoyancy in this study. By considering air as an inviscid fluid, the continuity and momentum equations [Eqs. (18) and (22)] are simplified as

$$\nabla\cdot\left(\rho\vec{U}\right)=0, \quad (25a)$$

$$\rho\left[\frac{\partial\vec{\boldsymbol{U}}}{\partial t}+\left(\vec{\boldsymbol{U}}\cdot\nabla\right)\vec{\boldsymbol{U}}\right]=-\nabla\vec{\boldsymbol{P}}+\rho\vec{g}. \quad (25b)$$

2.2.3 Energy equation

According to the first law of thermodynamics and the conservation of energy, the energy change rate of the element is equal to the sum of the net heat flux of heat into the element and the rate of work on the element via the body and surface forces, and source terms. The rate of work on the fluid element via the surface force is equal to the product of force and the components of velocity in the force direction (Fig. 4).

As indicated in Fig. 4, the fluid's internal energy and kinetic energy are expressed as

$$E_x = \rho u\left(e + \frac{1}{2}\vec{U}\cdot\vec{U}\right)dydz, \tag{26a}$$

$$E_y = \rho u\left(e + \frac{1}{2}\vec{U}\cdot\vec{U}\right)dxdz, \tag{26b}$$

$$E_z = \rho u\left(e + \frac{1}{2}\vec{U}\cdot\vec{U}\right)dxdy, \tag{26c}$$

$$E_{x,dx} = \left\{\rho u\left(e + \frac{1}{2}U^2\right) + \frac{\partial\left[\rho u\left(e + \frac{1}{2}U^2\right)\right]}{\partial x}dx\right\}dydz, \tag{26d}$$

$$E_{y,dy} = \left\{\rho v\left(e + U^2\right) + \frac{\partial\left[\rho u\left(e + \frac{1}{2}U^2\right)\right]}{\partial y}dy\right\}dxdz, \tag{26e}$$

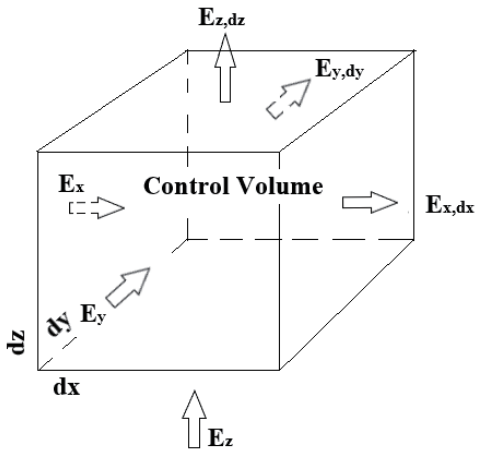

Fig. 4. Energy balance in cubic fluid element.

$$E_{z,dz} = \left\{ \rho w\left(e + \frac{1}{2}U^2 \right) + \frac{\partial\left[\rho v\left(e + \frac{1}{2}U^2 \right) \right]}{\partial z} dz \right\} dxdy. \tag{26f}$$

Integrating the fluid's internal energy and kinetic energy yields

$$dE = -\left\{ \frac{\partial\left[\rho u\left(e + \frac{1}{2}U^2 \right) \right]}{\partial x} + \frac{\partial\left[\rho u\left(e + \frac{1}{2}U^2 \right) \right]}{\partial y} + \frac{\partial\left[\rho v\left(e + \frac{1}{2}U^2 \right) \right]}{\partial z} \right\} dxdydz. \tag{27}$$

The total heat in the fluid's control volume [Eq.(4)] is expressed as

$$dQ = \left[\frac{\partial}{\partial x}\left(\lambda \frac{\partial T}{\partial x} \right) + \frac{\partial}{\partial y}\left(\lambda \frac{\partial T}{\partial y} \right) + \frac{\partial}{\partial z}\left(\lambda \frac{\partial T}{\partial z} \right) \right] dxdydz. \tag{28}$$

Considering the work of the fluid pressure and the normal and shear stresses on the element, the net works on the *x*-, *y*-, and *z*-axes are calculated as

$$dW_x = \left(-\frac{\partial P \cdot u}{\partial x} + \frac{\partial \sigma_{xx} \cdot u}{\partial x} + \frac{\partial \tau_{xy} \cdot v}{\partial x} + \frac{\partial \tau_{xz} \cdot w}{\partial x} \right) dxdydz, \tag{29a}$$

$$dW_y = \left(-\frac{\partial P \cdot v}{\partial y} + \frac{\partial \acute{o}_{yy} \cdot v}{\partial y} + \frac{\partial \tau_{yx} \cdot u}{\partial y} + \frac{\partial \tau_{yz} \cdot w}{\partial y} \right) dxdydz, \tag{29b}$$

$$dW_z = \left(-\frac{\partial P \cdot w}{\partial z} + \frac{\partial \sigma_{zz} \cdot w}{\partial z} + \frac{\partial \tau_{zx} \cdot u}{\partial z} + \frac{\partial \tau_{zy} \cdot v}{\partial z} \right) dxdydz. \tag{29c}$$

For energy conservation, the combustion heat ($\rho \cdot q_s$) and the pipe's friction force ($\mu \cdot \varnothing$) considering electromagnetic force ($K \cdot \Theta$) with Eqs. (26)–(29) yield

$$\begin{aligned} &\rho\left(\frac{\partial e}{\partial t} + u\frac{\partial e}{\partial x} + v\frac{\partial e}{\partial y} + w\frac{\partial e}{\partial z} \right) \\ &= \left[\frac{\partial}{\partial x}\left(\lambda \frac{\partial T}{\partial x} \right) + \frac{\partial}{\partial y}\left(\lambda \frac{\partial T}{\partial y} \right) + \frac{\partial}{\partial z}\left(\lambda \frac{\partial T}{\partial z} \right) \right] - p \cdot \nabla V + K \cdot V + \rho \cdot q_s + \mu \cdot \varnothing. \end{aligned} \tag{30}$$

The fluid element's internal energy is expressed as

$$e = c_p \cdot T - \frac{P}{\rho}, \tag{31}$$

where C_p is the specific heat at constant pressure.

Substituting Eq. (31) into Eq. (30) yields

$$\begin{aligned}\rho C_p\left(\frac{\partial T}{\partial t}+u\frac{\partial T}{\partial x}+v\frac{\partial T}{\partial y}+w\frac{\partial T}{\partial z}\right)&=\left[\frac{\partial}{\partial x}\left(\lambda\frac{\partial T}{\partial x}\right)+\frac{\partial}{\partial y}\left(\lambda\frac{\partial T}{\partial y}\right)+\frac{\partial}{\partial z}\left(\lambda\frac{\partial T}{\partial z}\right)\right]\\ &+\left(\frac{\partial P}{\partial t}+u\frac{\partial P}{\partial x}+v\frac{\partial P}{\partial y}+w\frac{\partial P}{\partial z}\right)+K\cdot V+\rho\cdot q_s+\mu\cdot\varnothing.\end{aligned} \tag{32}$$

Assuming that air density (ρ) is constant and neglecting the electromagnetic force ($K \cdot V$), combustion heat ($\rho \cdot q_s$), and radiation heat ($\mu \cdot \varnothing$), Eq. (32) in vector form is given as

$$\frac{\partial}{\partial t}\left(\rho C_p T\right)+\nabla\cdot\left(\rho C_p\vec{U}T\right)=\nabla\cdot\left(\lambda\nabla T\right)+\frac{\partial P}{\partial t}+\vec{\boldsymbol{U}}\cdot\nabla\vec{\boldsymbol{P}}+K\cdot V+\rho\cdot q_s+\mu\cdot\varnothing. \tag{33}$$

In the thermal flow field, the air density change is ignored. In this case, ρ is constant. $\partial P/\partial t$ and $\vec{\boldsymbol{U}}\cdot\nabla\vec{\boldsymbol{P}}$ have minimal impact and thus are also ignored. $K \cdot V$ is also ignored. Regarding viscous dissipation, $\mu \cdot \varnothing$ is ignored except for high-speed flows or significant shear. $\rho \cdot q_s$ is simplified to a general source term S, which represents various heat source effects. On the basis of the fundamentals of heat and mass transfer, Eq. (33) is given as[34]

$$\frac{\partial}{\partial t}\left(\rho C_p \mathrm{T}\right)+\nabla\cdot\left(\rho C_p\vec{\boldsymbol{U}}T\right)=\nabla\cdot\left(\lambda\nabla T\right)+S\cdot \tag{34}$$

2.3 Semi-implicit method for pressure-linked equation (SIMPLE)

Thermal simulation and fluid dynamic analysis are used to estimate thermal dissipation. Thus, SIMPLE was employed for heat convection calculation in this study.

The SIMPLE process is as follows.

(Step A) Initial guess of the pressure field P^* and velocity field U^*

(Step B) Momentum equation

For a steady flow in thermal dissipation, Eq. (24b) is simplified as

$$\rho\left(\vec{\boldsymbol{U}}\cdot\nabla\right)\vec{\boldsymbol{U}}=\rho\vec{g}-\nabla\vec{\boldsymbol{P}} \tag{35a}$$

or

$$[\boldsymbol{A}]\vec{\boldsymbol{U}} = \boldsymbol{b} - \nabla\vec{\boldsymbol{P}}. \tag{35b}$$

The guessed pressure field P^* is used to solve the momentum equations and obtain the temporary velocity field U^*.

$$AU^* = b - \nabla P^* \tag{36}$$

(Step C) Pressure correction

Using Eq. (24a) and ignoring the change in air density in forcing flow,

$$\nabla \cdot \left(\vec{U}\right) = 0. \tag{37}$$

The relationship between P' and U' is given as

$$\nabla \cdot \left(U^* + U'\right) = 0, \tag{38}$$

where $U' = -\nabla P'$.

(Step D) Pressure and velocity updates

$$P = P^* + P', \tag{39a}$$

$$U = U^* + U'. \tag{39b}$$

(Step E) Repeat steps B to D until convergence

We created the SIMPLEST algorithm by incorporating the skew transport into the SIMPLE algorithm (Fig. 5). In the algorithm, we considered the skew transport in SIMPLE [Eq. (40)],

$$\nabla \cdot \left(\rho C_p \vec{\boldsymbol{U}} T\right), \tag{40}$$

where ρ is the air density, C_p is the specific heat capacity at constant pressure, $\vec{\boldsymbol{U}}$ is the velocity vector of the fluid, and T is the temperature.

In this study, the SIMPLEST algorithm was used to correct velocity and pressure until differences between calculated and measured values reached a predetermined value. Then, the obtained pressure and velocity were used to calculate temperature. The Flotherm convergence conditions were met when the ratio of the deviation to the previous values of pressure, velocity, and temperature reached 0.5%, at which point the calculation was terminated, or when the number of iterations reached 3000.

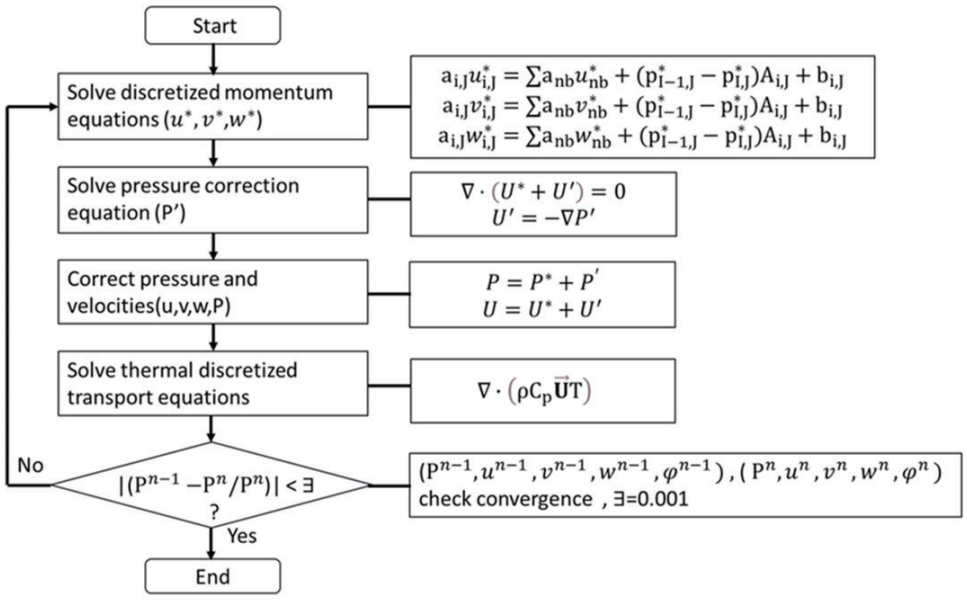

Fig. 5. SIMLEST algorithm.

3. Model Design and Verification

The laptop computer used in this study featured a bottom-mounted cooling system with a heat pipe of 8.0 mm diameter. The radiator was made of copper. A thermal model for the laptop computer was established using 3D CAD (Computer Aided Design) models and CFD software with verification conditions including ambient temperature and workload. Simulated temperatures were compared with measured ones to evaluate the accuracy.

3.1 Thermal model

The model setting and the positioning of the heat transfer components are shown in Fig. 6.

The dimensions of the laptop computer were 310 × 225 × 20 mm (width × length × height). The weight was smaller than 2 kg. The specifications of the computer are described in Table 1. The body was made of aluminum alloy, which is lightweight, and strong, and has a high thermal conductivity. There was a cooling vent at the bottom for forced cooling and heat dissipation. The cooling components included a fan, heat pipes, and heat fins. The dimensions of the fan were 87 × 87 × 6.0 mm and the blade thickness was 0.15 mm. The fan blades were made of liquid crystal polymers, and the fan contained a fluid dynamic bearing, copper sleeve, bonded NdFeB magnet, and three-phase motor. The diameter and length of the heat pipe were 8.0 and 294.2 mm, respectively. The material of the fins was pure copper (C1100) with the dimensions of 87.6 × 20 × 6.18 mm, and its thickness was 0.1 mm. The thermal paste of the cooler had a thermal conductivity (K) of 5, and the power consumption of the CPU was 22W (Table 1).

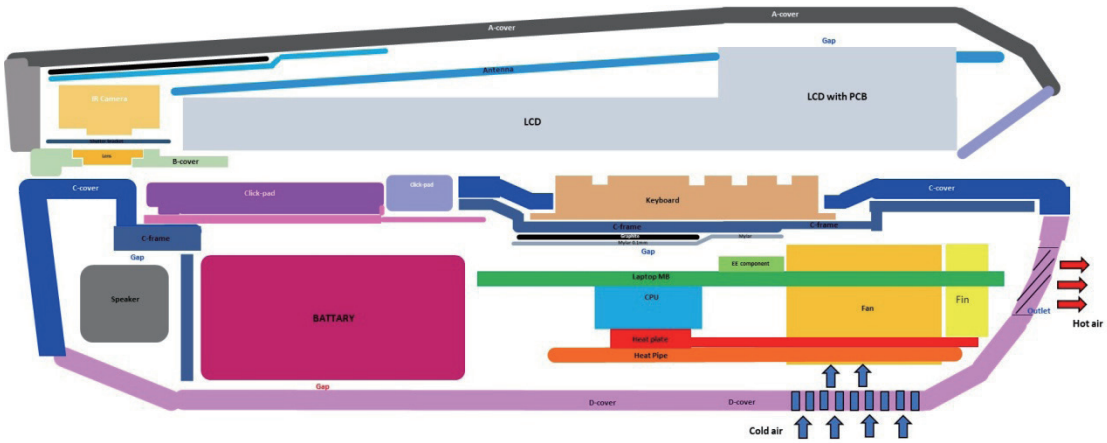

Fig. 6. (Color online) Model structure of heat transfer components of laptop computer.

Table 1
Simulated temperatures and errors (compared with measured temperature) at different meshes.

Number of meshes	Simulated temperature (°C)	Difference from measured temperature (%)
70000	74.7	11.4
400000	68.7	2.5
7000000	67.6	0.9

3.2 Mesh count and accuracy

We used three different numbers of meshes to simulate the temperature of the CPU: 70000, 400000, and 7000000 meshes (Fig. 7).

We constructed a thermal conduction model for simulation. The simulation was conducted using CFD and turbulence modeling using the k-ε model. We calculated the accuracy of the simulation using the temperature gradient of Intel Xeon® CPU Max 9462. The simulated temperatures are shown in Table 1.

To verify the simulation result, we measured the temperature of the keyboard. We used an infrared camera to measure the temperature distribution on the keyboard surface. The simulated and measured temperatures are shown in Fig. 8.

The simulation temperature matched the measured ones. The hottest area of the keyboard was located near the ESC, F12, and power buttons. The temperature gradient was apparent. The simulated CPU temperature at 70000 meshes was 74.7 °C with a difference of 11.4% from the measured temperature of 67.0 °C. At 400000 and 7000000 meshes, the difference was 0.9%. Despite the decreased difference, the required computational time was longer for 400000 and 7000000 meshes than for 70000 meshes. We selected 400000 meshes for the simulations in the subsequent analysis considering computational time and accuracy.

4. Parameter Analysis

The cooling mechanism of the laptop computer involved forced convection to dissipate heat using the fins of the heat sink (Fig. 9). The designs of the air outlet and fins are depicted in Fig. 10.

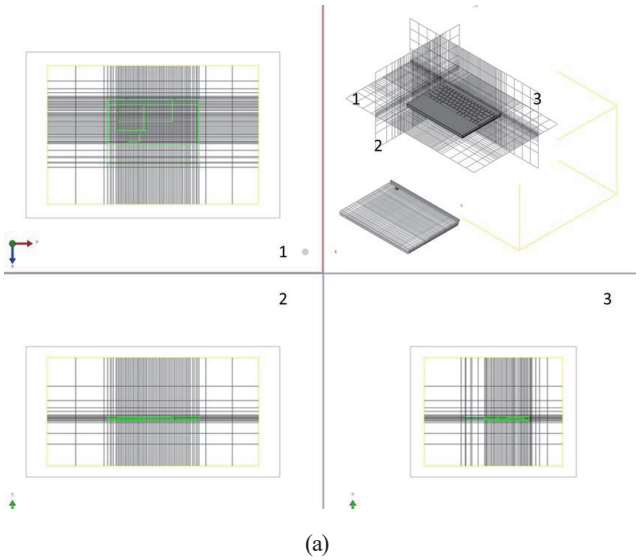

(a)

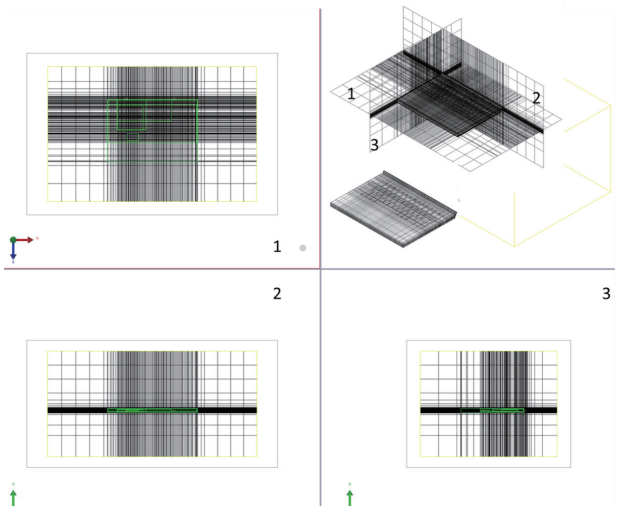

(b)

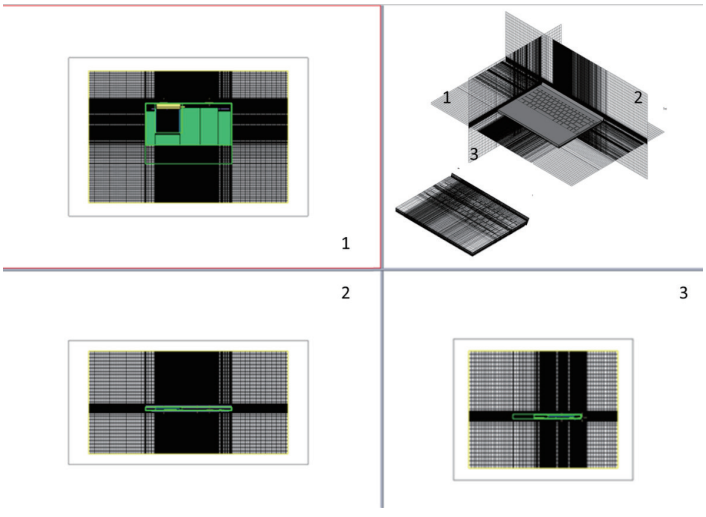

(c)

Fig. 7. (Color online) Numbers of meshes in the simulation of temperature: (a) 70000, (b) 400000, and (c) 7000000 meshes.

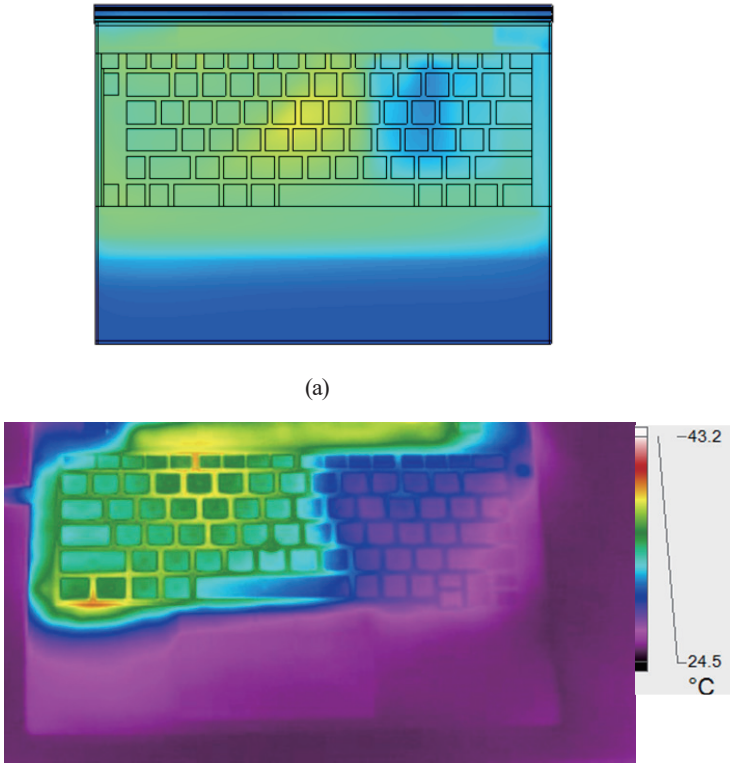

(a)

(b)

Fig. 8. (Color online) Simulated and measured temperatures of keyboard at 400000 meshes: (a) Simulated and (b) measured temperatures.

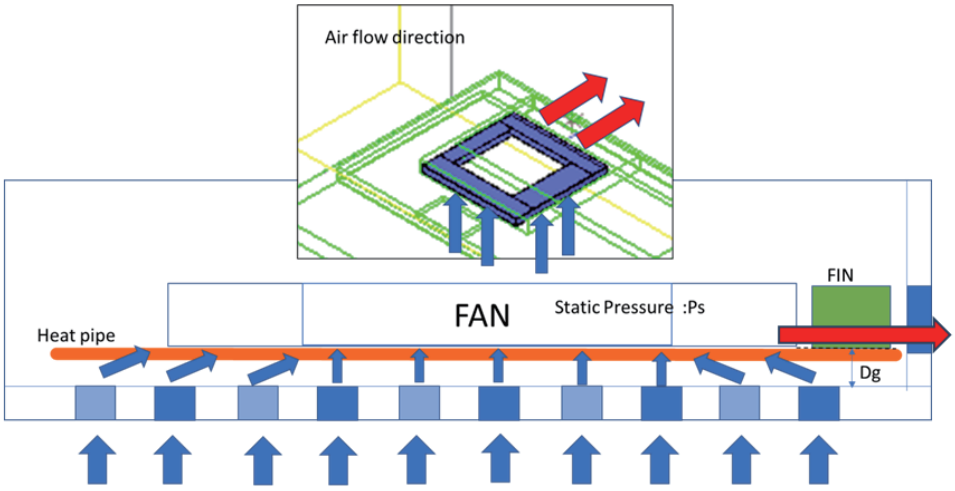

Fig. 9. (Color online) Mechanism of forced convection.

The distance (D_g) between the fan and the air inlet affects the pressure loss, airflow rate, and cooling efficiency. This topology of the airflow path is important as it affects the cooling efficiency. With the number and height of the outlet unchanged, the width of the outlet (H_d) was adjusted. The constraint condition was $H_d < H$, where H is a fixed value. To enhance the thermal

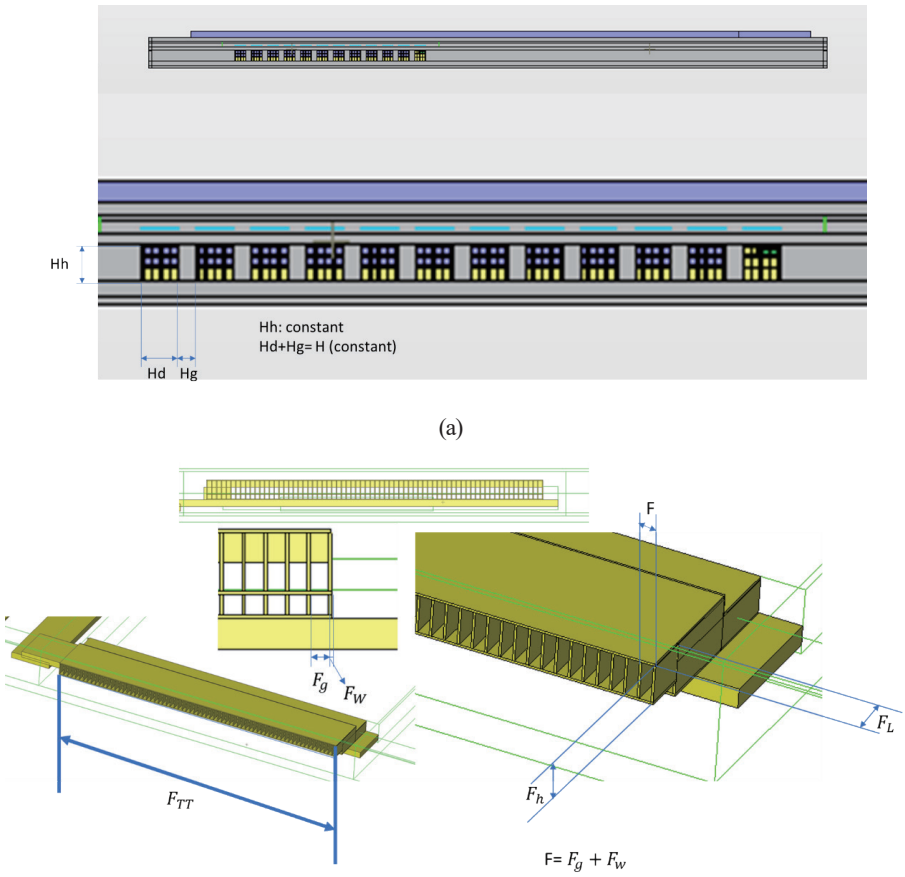

Fig. 10. (Color online) Designs of air outlet and fins: (a) Air outlet and (b) fins.

conductivity and cooling effect, cooling fins were added at the outlet. When the length, width, height, spacing, and total length of the cooling fins are F_L, F_w, F_h, F_g, and F_{TT}, respectively, the number of cooling fins (F_N) is $F_{TT}/(F_w + F_g)$. F_w and F_h are fixed values, and the length of a single cooling fin module is $F = F_w + F_g$. In the design of the cooling fins, F_L and F_g were varied. Since the cooling mechanism involves forced convection, the selection of the fan's static pressure P_s is important. To optimize the design, a sensitivity analysis was conducted for D_g, P_s, H_d, F_L, and F_N. The relationships of the parameters to the CPU temperature are shown in Fig. 11. The specifications of the fan are listed in Table 2.

As H_d increased, the CPU temperature decreased. With a diameter of 4.9 mm, the alignment between the inlet and the fin became optimal for cooling. When the size of the opening increased, pressure loss occurred between the fin and the inlet, increasing the CPU temperature. When the length of the fins increased, the gap between the fins and the outlet became narrower. The increase in pressure loss owing to the increase in fin length was smaller than the reduction in pressure loss at the narrower gap, which decreased pressure loss. Thus, as the fan's airflow increased, the cooling effect improved. The CPU temperature varied with H_d. H_d affected the outlet airflow. On adjusting the air outlet width to 4.9 mm, the CPU temperature was reduced to 62.1 °C. The CPU temperature was proportional to Ps; the larger the Ps of the fan, the lower the

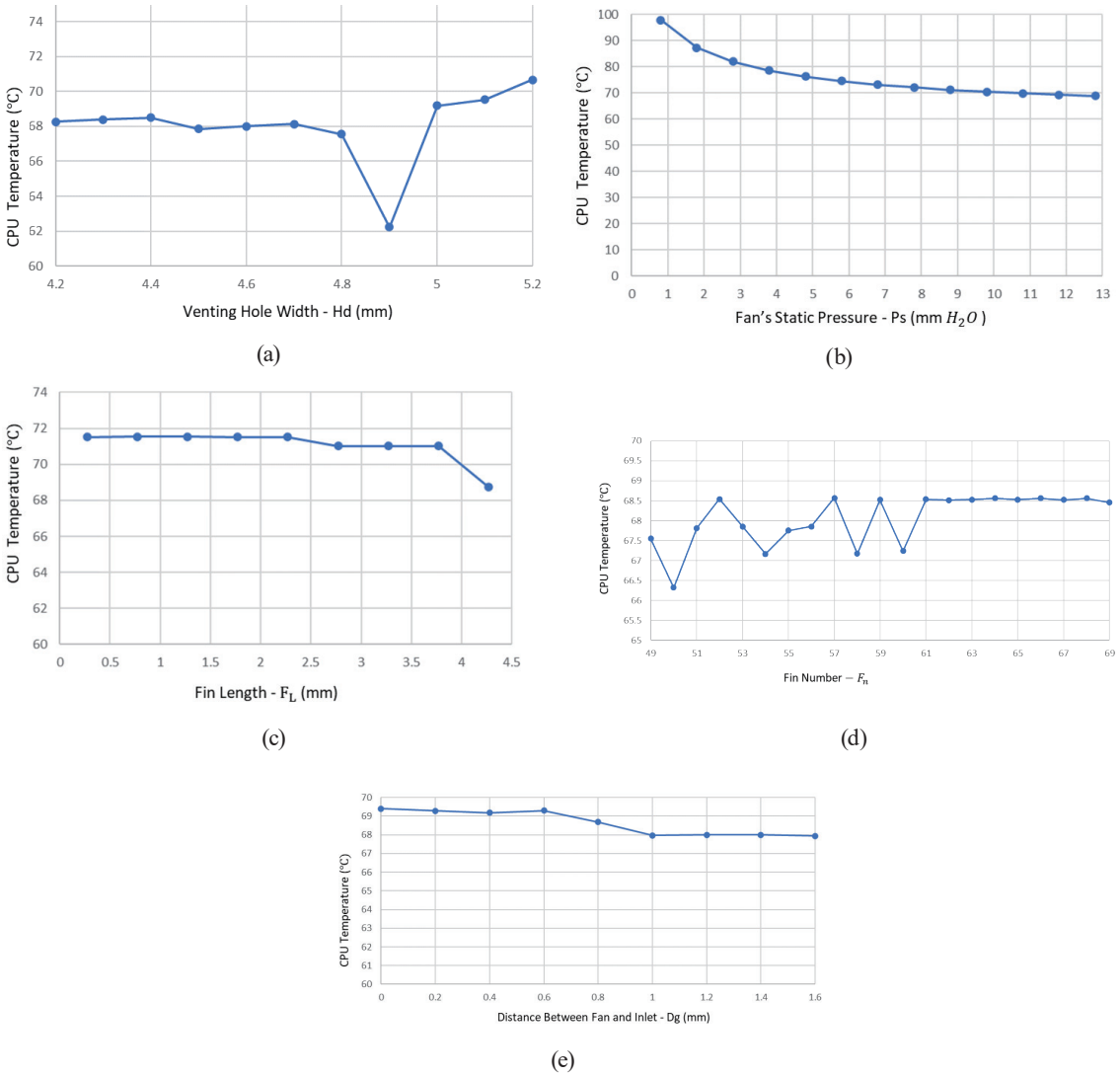

Fig. 11. (Color online) Relationships of parameters with CPU temperature: (a) H_d, (b) P_s, (c) F_L, (d) F_N, and (e) D_g.

Table 2
Specifications of fan of laptop computer.

Item	Specification
Direction of fan rotation	Counterclockwise
Rated voltage	5.0 V
Starting voltage or duty	20% at 5 V
Safe current	5 A
Maximum power at 4000 RPM	2.5 W
Fan speed (RPM) at 5V	4000 ± 7%
Fan speed (RPM) at start	1350 ± 200
Maximum static pressure without air	12.8 (minimum: 11.9)
Rated flow without air	5.5 cubic feet per minute (CFM)
Insulation resistance	10 MΩ at 500 V

CPU temperature. The CPU temperature also varied with F_L. When F_L was adjusted to 4.25 mm, the CPU temperature decreased to 57.2 °C. When F_N was adjusted to 50, the CPU temperature was reduced to 66.25 °C. Even when F_N exceeded 61, F_{TT} remained constant. When F_N increased, F decreased, which means that F_g affected heat dissipation. When F_N reached a certain value, small F_g caused low heat dissipation, resulting in the CPU temperature of 68.5 °C. The CPU temperature decreased as D_g increased. Increasing D_g decreased the pressure loss at the inlet, which increased the airflow and decreased the CPU temperature. When D_g was adjusted to 890.9 mm, the CPU temperature was reduced to 60.9 °C.

Such results showed that D_g, P_s, H_d, F_L, and F_N affected the CPU temperature as they affected the overall cooling effect. Therefore, D_g, P_s, H_d, F_L, and F_N were selected as parameters for the optimization of the cooling system of the laptop computer in this study.

5. Optimization of Cooling System

The optimization process of the cooling system is shown in Fig. 12. On the basis of the selected values of the parameters (Table 3), 216 scenarios were reviewed in the first stage of optimization. The corresponding parameters for the lowest CPU temperature (T_{CPU}) were then identified. The iteration results showed that at the 80th, 105th, and 129th iterations, T_{CPU} reached the lowest temperature of 64 °C (Fig. 13). The results of the optimization of the parameters by the predetermined number of iterations were 1 mm, 12.8 mmH_2O, 4.7 mm, 3.0 mm, and 69 mm for D_g, P_s, H_d, F_L, and F_N, respectively (Fig. 14).

We added two values of H_d and three values to P_s for the second stage of optimization (Table 4). With various combinations of the parameters, we reviewed 540 scenarios (Fig. 15). At the

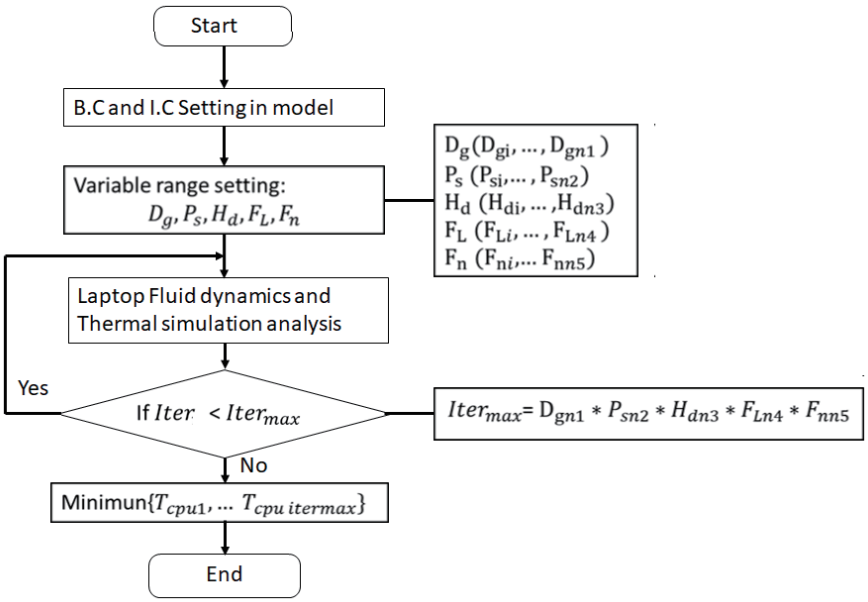

Fig. 12. Optimization process for cooling system.

Table 3
Parameters selected for first stage of optimization.

Parameter	Value range (minimum, average, maximum)
H_d	(4.2, 4.7, 5.2)
P_S	(11.8, 12.3, 12.8)
F_N	(59, 64, 69)
D_g	(0.5, 1.0, 1.5)
F_L	(1, 2, 3, 4)

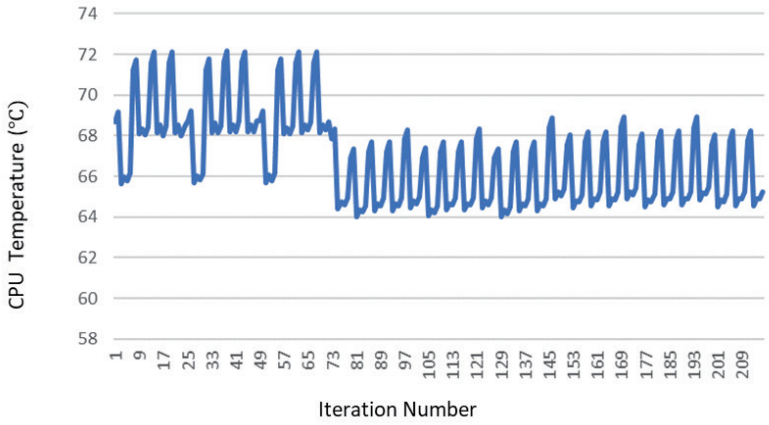

Fig. 13. (Color online) Iteration results of CPU temperature in first stage of optimization.

324th, 362nd, and 400th iterations, T_{CPU} reached the lowest temperature of 59.6 °C. At T_{CPU}, the values of D_g, H_d, F_L, and F_N were 1, 4.9, 4.0, and 69 mm, respectively (Fig. 16). After refining the parameters, T_{CPU} became lower in the second stage of optimization than in the first stage. H_d affected the pressure loss and heat dissipation so it needed to be selected to minimize pressure loss. As T_{CPU} was affected by F_L and F_N, streamlined heat dissipation fins reduced pressure loss, enabling effective cooling. However, an excessive number of fins under a fixed length increased pressure loss, which degraded heat dissipation. D_g affected the pressure loss at the inlet. When D_g decreased, the shape factor of the pressure loss and flow velocity pressure loss increased, which is unfavorable for heat dissipation. Therefore, a larger D_g is preferable.

The final optimization results were 1.0 mm, 12.8 mmH_2O, 4.9 mm, 4.0 mm, and 69.0 mm for D_g, P_s, H_d, F_L, and F_N, respectively. The optimized D_g and P_s increased pressure loss, while the optimized H_d minimized it. F_L and F_N were selected to minimize pressure loss in the airflow. To explore the effect of thermal dissipation at a constant T_{CPU}, the ambient temperatures of 25, 30, and 35 °C were chosen for the experiment in this study.

6. Stable CPU Temperature

At an ambient temperature of 25 °C, the optimized values of D_g, P_s, H_d, F_L, and F_N were 1.0 mm, 12.8 mmH_2O, 4.9 mm, 4.0 mm, and 69.0 mm, respectively. The speed of the fan was 3000 RPM, and the maximum temperature of the CPU was 59.1 °C. At 30 °C, the optimized values of

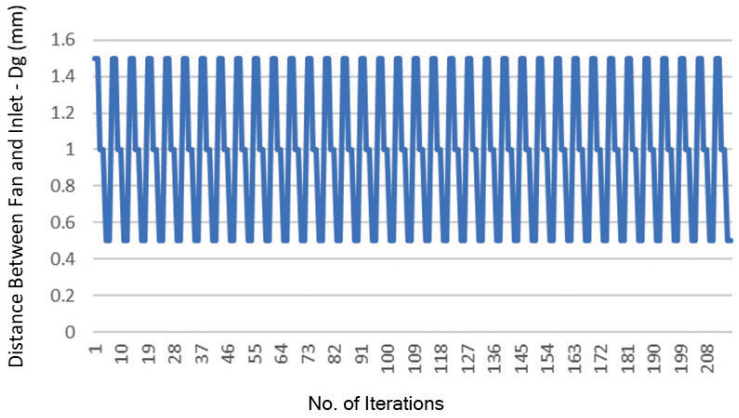

(a)

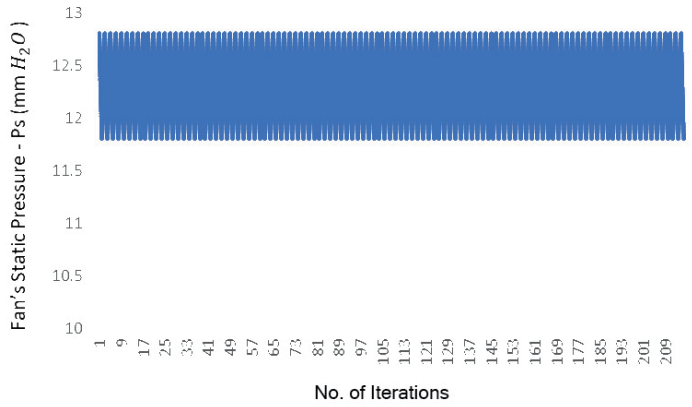

(b)

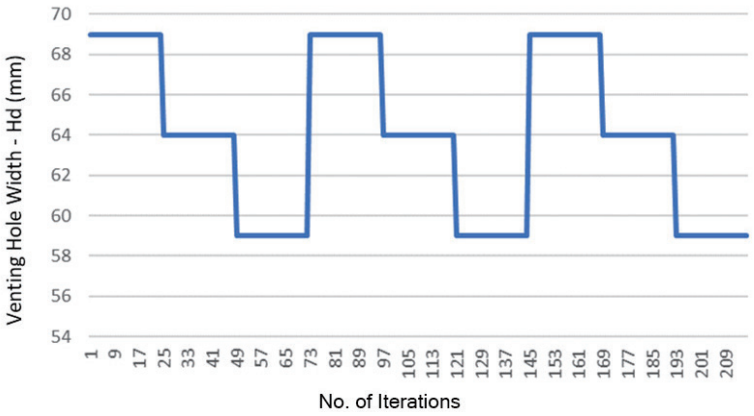

(c)

Fig. 14. (Color online) Optimization of parameters through iteration in first stage of optimization: (a) iteration of D_g, (b) iteration of P_s, (c) iteration of H_d, (d) iteration of F_L, and (e) iteration of F_N.

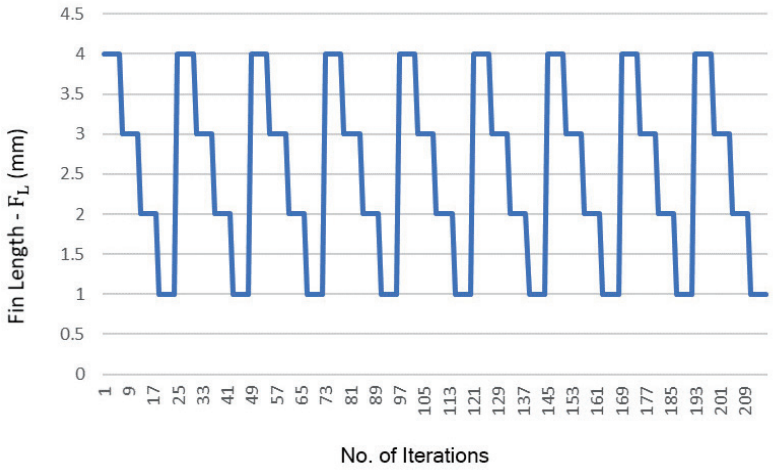

(d)

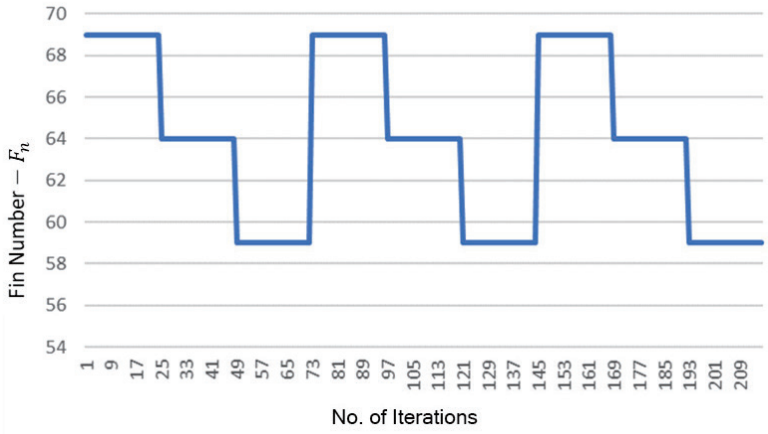

(e)

Fig. 14. (Continued) (Color online) Optimization of parameters through iteration in first stage of optimization: (a) iteration of D_g, (b) iteration of P_s, (c) iteration of H_d, (d) iteration of F_L, and (e) iteration of F_N.

Table 4
Parameters selected for second stage of optimization.

Parameter	Value range (minimum, average, maximum)
H_d	(4.8, 4.9, 5.0, 5.1, 5.2)
F_N	(59, 64, 69)
P_S	(10.8, 11.8, 12.8)
D_g	(0.5, 1.0, 1.5)
F_L	(1,2, 3, 4)

D_g, H_d, F_L, and F_N were 1.0, 4.9, 4.0, and 69.0 mm with P_s of 16.8 mmH_2O at a speed of 4000 RPM. Then, the CPU temperature was maintained at 60.1 °C. At the ambient temperature of 35 °C and P_s of 20.8 mmH_2O (4000 RPM), the CPU temperature increased to 67.1 °C.

Maintaining the CPU within an optimal temperature range is essential for ensuring proper

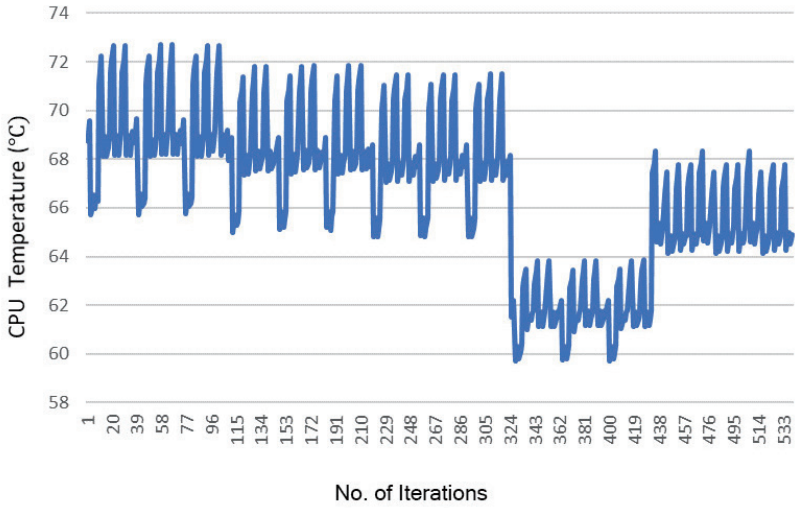

Fig. 15. (Color online) Iteration results of CPU temperature in second stage of optimization.

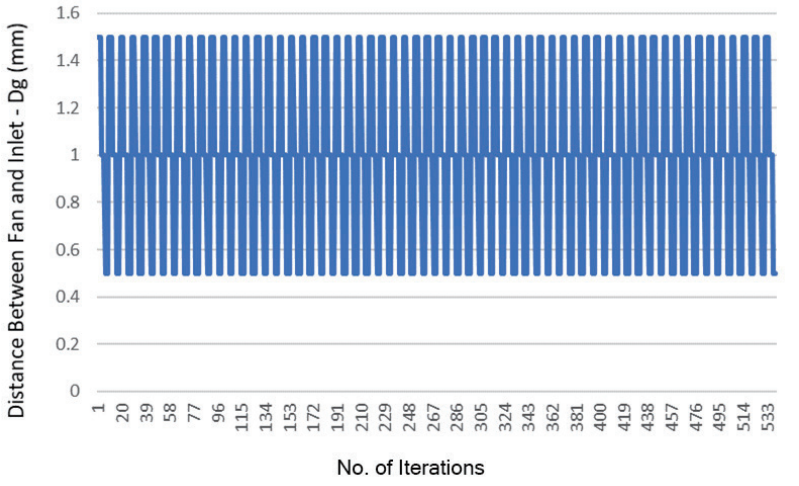

(a)

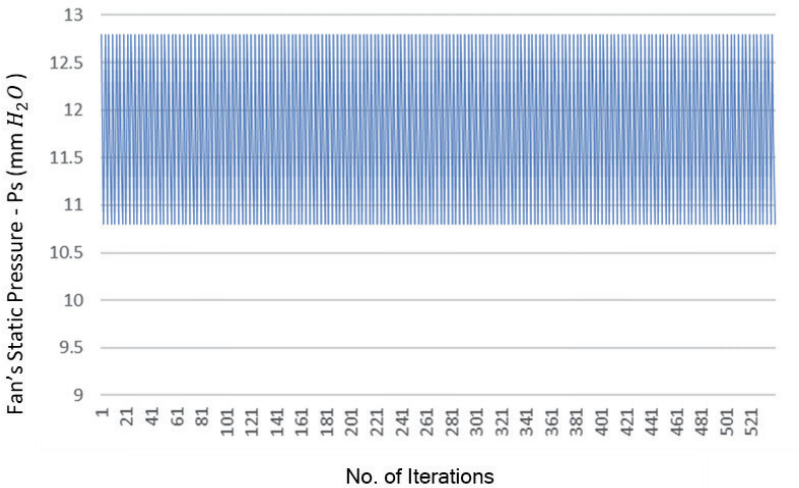

(b)

Fig. 16. (Color online) Optimization of parameters through iterations in second stage of optimization: (a) iteration of D_g, (b) iteration of P_s, (c) iteration of H_d, (d) iteration of F_L, and (e) iteration of F_N.

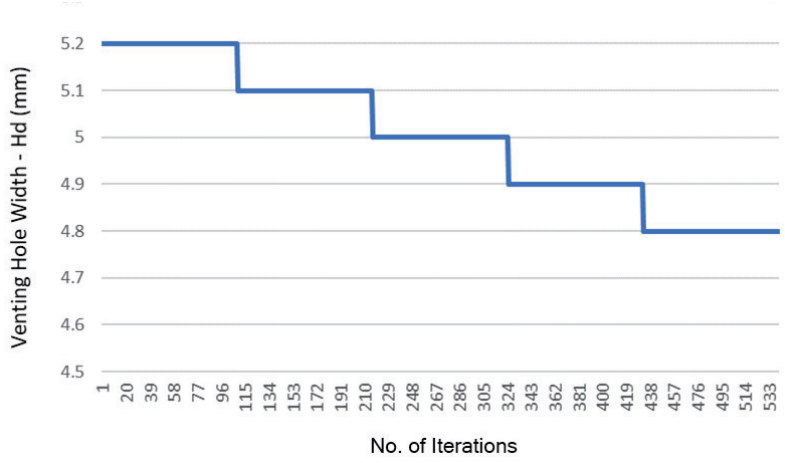

(c)

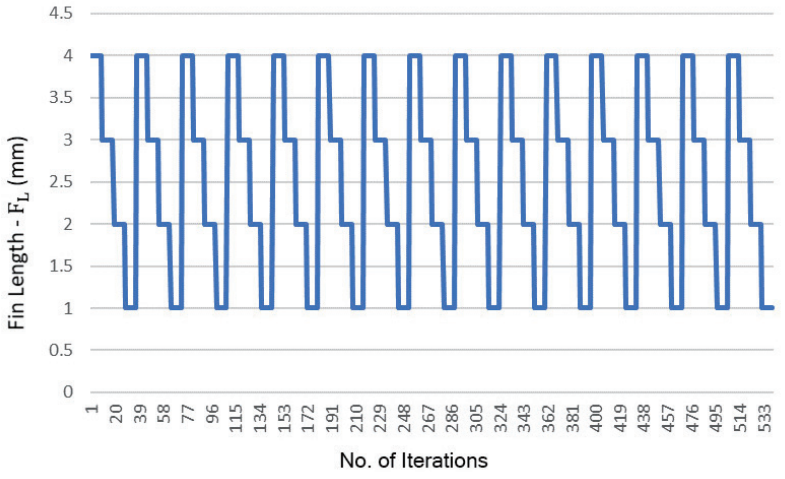

(d)

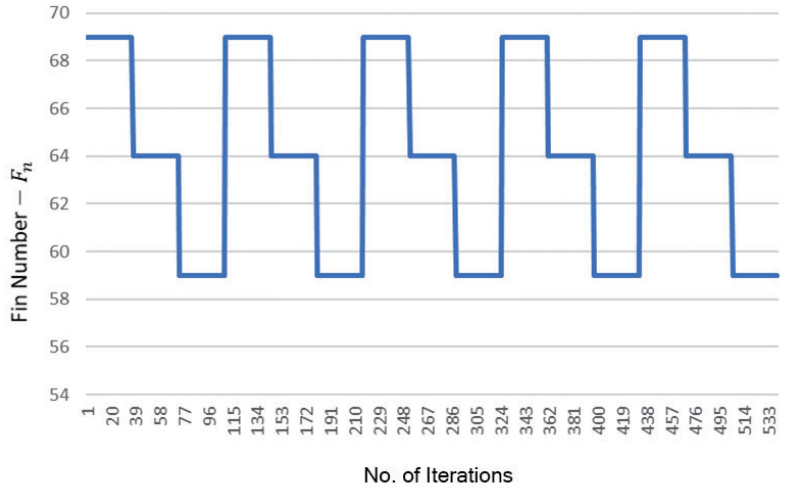

(e)

Fig. 16. (Continued) (Color online) Optimization of parameters through iterations in second stage of optimization: (a) iteration of D_g, (b) iteration of P_s, (c) iteration of H_d, (d) iteration of F_L, and (e) iteration of F_N.

performance. A CPU temperature of 67.1 °C is generally acceptable.[34] With the parameter (D_g, H_d, F_L, and F_N) values of 1.0, 4.9, 4.0, and 69.0 mm, the simulation results showed T_{CPU} values of 67.4 and 67.3 °C at ambient temperatures of 25 and 30 °C, respectively. For P_s and T_{CPU}, 22.8 mmH_2O and 67.1 °C were appropriate for the design of the cooling system. T_{CPU} values at fan speeds of 2800, 3200, and 4000 RPM at ambient temperatures of 25, 30, and 35 °C are shown in Fig. 17.

7. Optimized Design of Cooling System

To maintain T_{CPU} of 67.1 °C at various ambient temperatures, the automatic control of the fan speed is necessary. In this study, an Arduino-based controlling system including sensors and a controller was constructed (Fig. 18) on the basis of the control mechanism shown in Fig. 19. The fan speed was adjusted to 2800 RPM when the ambient temperature was lower than or equal to

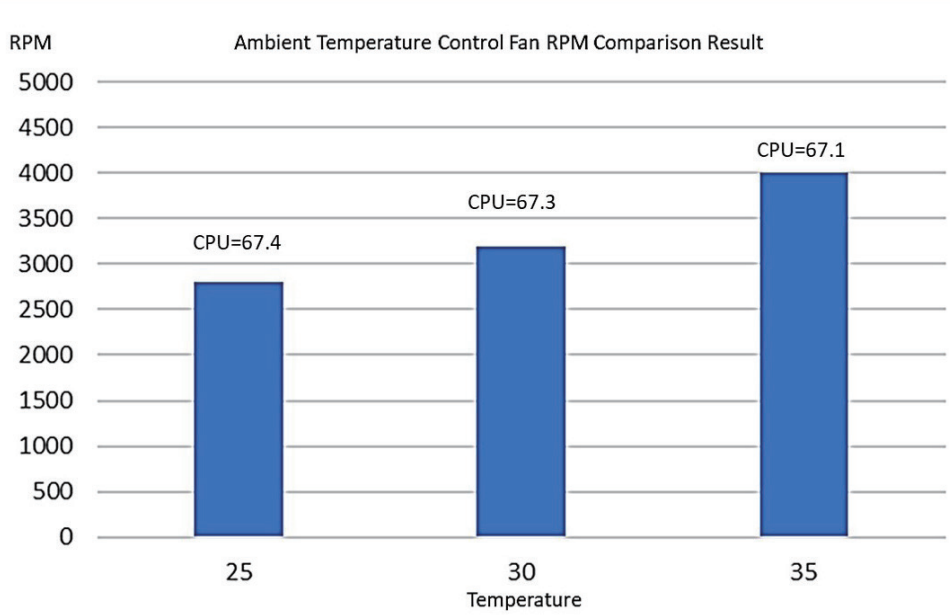

Fig. 17. (Color online) T_{CPU} at ambient temperatures of 25, 30, and 35 and fan speeds of 2800, 3200, and 4000 RPM.

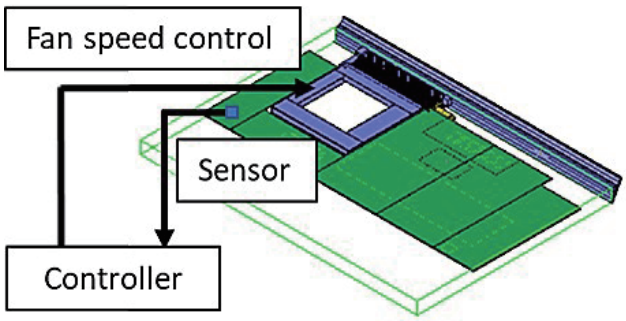

Fig. 18. (Color online) Arduino-based control system.

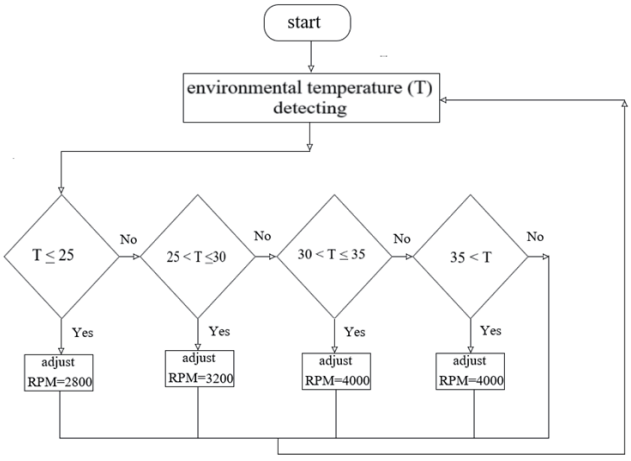

Fig. 19. Diagram of fan speed control in accordance with ambient temperature using thermal sensor.

25 °C. The speed was adjusted to 3200 RPM when the ambient temperature exceeded 25 °C but was lower than or equal to 30 °C. When the temperature exceeded 30 °C but remained below or equal to 35 °C, the fan speed was set to 4000 RPM. When the ambient temperature exceeded 35 °C, the fan speed was maintained at 4000 RPM.

To maintain T_{CPU} at 67.1 °C and the maximum P_s of 22.8 mmH_2O, the specifications of the fan were determined to be as presented in Table 5. At an ambient temperature of 25 °C and a target T_{CPU} of 67.4 °C, the required fan speed was 2800 RPM. At an ambient temperature of 30 °C and a target T_{CPU} of 67.3 °C, the required fan speed was 3200 RPM.

The relationship between the flow rate and the fan speed is described by similarity laws, which are used to predict the performance of a fan under different operating conditions. The flow rate (Q) of the fan is related to the fan speed. This relationship follows the proportional law[35,36]

$$\frac{Q_1}{Q_2} = \frac{N_1}{N_2}, \tag{41}$$

where Q_1 and Q_2 represent the fan's flow rates at speeds N_1 and N_2, respectively.

As the fan speed increases, the flow rate also increases. The logic for adjusting the fan speed in accordance with ambient temperature was programmed into the controller. The ambient temperature affects the cooling system of the laptop computer. At a high temperature, if the fan speed is not adjusted in time, the GPU temperature rises rapidly, leading to a decrease in system performance. Through optimization, the fan speed is determined in accordance with the ambient temperature to effectively maintain a stable temperature and ensure an effective operation.

Consequently, other laptop research studies have primarily focused on developing new composite cooling materials to enhance heat dissipation efficiency, though this strategy increases costs. In contrast, we optimize the topology of cooling channels to improve the laptop cooling performance. Furthermore, we integrate an intelligent system to adjust fan speed, making our proposed methods both effective and cost-efficient.

Table 5
Specifications of selected fan.

Item	Specification
Minimum start voltage or duty	20% at 12 V
Safety certification current	0.07–1.48 A
Maximum power at 4000 RPM	5 W at 4000 RPM
Fan speed (RPM) at 5 V	4000 ± 7%
Fan speed (RPM) at start	1500 ± 200
Maximum fan static pressure without air	22.8 (Minimum: 20.8)
Rated flow without air	8.4 CFM
Insulation resistance	10 MΩ at 500

8. Conclusions

We optimized the cooling system of a laptop computer to ensure a stable CPU temperature. Since the CPU temperature is the highest among the components, it needs to be controlled for optimal operation. We analyzed the distance between the fan and intake (D_g), fan static pressure (P_s), outlet width (H_d), heat dissipation fin length (F_L), and the number of heat dissipation fins (F_N) as they significantly impact the CPU temperature. The parameters were optimized at different ambient temperatures (25, 30, and 35 °C), and the CPU temperature was maintained at a value lower than 67.1 °C. The fan speed was recommended to be 2800, 3200, and 4000 RPM with a static pressure of 22.8 mmH_2O. In the study presented in this paper, we first conducted a sensitivity analysis of cooling channel topology parameters to determine the optimal parameters for engineering heat dissipation. In the numerical analysis, an appropriate number of mesh points was used to ensure accuracy while balancing computational time costs. We successfully identified the optimal design values for cooling channel topology parameters. Furthermore, an intelligent system was implemented to adjust fan speed, effectively enhancing the laptop cooling efficiency. The numerical analysis results confirmed the effectiveness of this approach. In future work, further improvements in laptop cooling methods can be explored, such as replacing heat pipes with a water-cooling system or a hybrid system to enhance cooling efficiency.

References

1 H. Y. Zhang, D. Pinjala, O. K. Navas, M. Iyer, P. Chan, X. P. Liu, H. Hayashi, and J. Han: ITherm 8th Intersociety Conf. Thermal and Thermomechanical Phenomena in Electron Systems (2002) 1012489. https://doi.org/10.1109/ITHERM.2002.1012489
2 M. K. Berhe: ASME 2007 Int. PACK Conf. (2007) 1041. https://doi.org/10.1115/IPACK2007-33873
3 J. J. Esplin, J. K. Boyle, S. D. Sommerfieldt, and K. L. Gee: J. Acoust. Soc. Am. **130** (2011) 2564. https://doi.org/10.1121/1.3655272
4 L. Richter, M. Lehna, S. Marchand, C. Scholz, A. Dreher, S. Klaiber, and S. Lenk: Renewable and Sustainable Energy Rev. **163** (2022) 112459. https://doi.org/10.1016/j.rser.2022.112459
5 E. M. Dede: J. Electronic Packaging **134** (2012) 041001. https://doi.org/10.1115/1.4007159
6 Y. Deng and Y. Jiang: Appl. Therm. Eng. **199** (2021) 117555. https://doi.org/10.1016/j.applthermaleng.2021.117555
7 A. Bejan: Advanced Engineering Thermodynamics (John Wiley & Sons, 2016). https://doi.org/10.1002/9781119245964
8 Y. A. Cengel: Heat Transfer – A Practical Approach, (Tata McGraw-Hill, 2023) 2nd ed. https://spada.uns.ac.id/pluginfile.php/150729/mod_label/intro/ebook_a_cengel.pdf
9 B. Güler: Heat Transfer **53** (2024) 2864. https://doi.org/10.1002/htj.23058
10 H. Xie, A. Ali, and R. Bhatia: ITherm'98. 6th Intersociety Conf. Thermal and Thermomechanical Phenomena in Electronic Systems (1998) 442. https://doi.org/10.1109/ITHERM.1998.689600

11 M. Mochizuki, Y. Saito, K. Goto, T. Nguyen, P. Ho, M. Malcolm, and M. Morando: Thirteenth IEEE SEMI-THERMTM Symp. (1997) 64. https://doi.org/10.1109/STHERM.1997.566784
12 S. Wang, R. Tu, X. Chen, X. Yang, and K. Jia: Appl. Therm. Eng. **222** (2023) 119817. https://doi.org/10.1016/j.applthermaleng.2022.119817
13 A. M. Adham, N. Mohd-Ghazali, and R. Ahmad: Renewable and Sustainable Energy Rev. **21** (2013) 614. https://doi.org/10.1016/j.rser.2013.01.022
14 M. P. Bendsøe and O. Sigmund: Topology Optimization (Springer, 2004). https://doi.org/10.1007/978-3-662-05086-6
15 M. A. Rahman, S. M. M. Hasnain, P. Paramasivam, and A. G. Ayanie: RSC Advances **14** (2024) 31291. https://doi.org/10.1039/d4ra05845c
16 R. Arunkumar: IOSR J. Electrical and Electronics Engineering **12** (2017) 1. https://doi.org/10.9790/1676-1203040108
17 A. R. Maher and S. Al-Baghdadi: Int. J. Energy and Env. **11** (2020) 145.
18 X. Zhang, Y. Liu, M. Halbig, M. Singh, A. Almansour, and Y. Zheng: Appl. Therm. Eng. **254** (2024) 123912. https://doi.org/10.1016/j.applthermaleng.2024.123912
19 P. Taddeo, J. Romaní, J. Summers, J. Gustafsson, I. Martorell, and J. Salom: Appl. Therm. Eng. **234** (2023) 121260. https://doi.org/10.1016/j.applthermaleng.2023.121260
20 W. M. Sheng, A. M. Elfaghi, and L. O. Afolabi: J. Advanced Research in Fluid Mechanics and Thermal Sciences **99** (2022) 58. https://doi.org/10.37934/arfmts.99.1.5865
21 S. K. Pathak, R. Kumar, V. Goel, A. K. Pandey, and V. V. Tyagi: Appl. Therm. Eng. **216** (2022) 119023. https://doi.org/10.1016/j.applthermaleng.2022.119023
22 G. Colangelo, E. Favale, M. Milanese, A. de Risi, and D. Laforgia: Appl. Therm. Eng. **127** (2017) 421. https://doi.org/10.1016/j.applthermaleng.2017.08.042
23 D. Sahel, L. Bellahcene, A. Yousfi, and A. Subasi: Int. Comm. in Heat and Mass Transfer **122** (2021) 105133. https://doi.org/10.1016/j.icheatmasstransfer.2021.105133
24 J. Wu, H. Liu, C. Li, C. Li, and G. Xie: Appl. Therm. Eng. **254** (2024) 123922. https://doi.org/10.1016/j.applthermaleng.2024.123922
25 S. Ghosh, I. Chatterjee, K. Ghosh, S. Hore, R. Ranjan, and S. Debnath: AIP Conf. Proc. **2764** (2023) 070010. https://doi.org/10.1063/5.0144156
26 M. Ismail: Int. J. Thermofluids **23** (2024) 100737. https://doi.org/10.1016/j.ijft.2024.100737
27 J. D. Deaton and R. V. Grandhi: Struct. Multidiscip. Optim. **49** (2014) 1. https://doi.org/10.1007/s00158-013-0956-z
28 S. B. Dilgen, C. B. Dilgen, D. R. Fuhrman, O. Sigmund, and B. S. Lazarov: Struct. Multidiscip. Optim. **57** (2018) 1905. https://doi.org/10.1007/s00158-018-1967-6
29 Z. Yuan and A. K. Coskun: iScience **25** (2022) 103582. https://doi.org/10.1016/j.isci.2021.103582
30 Z. Wang, C. Bash, N. Tolia, M. Marwah, X. Zhu, and P. Ranganathan: ASME 2009 InterPACK Conf. **2** (2009) 709. https://doi.org/10.1115/InterPACK2009-89074
31 A. Iranfar, F. Terraneo, G. Csordás, M. Zapater, W. Fornaciari, and D. Atienza: Design, Automation and Test in Europe Conf. and Exhibition (2020) 642. https://doi.org/10.23919/DATE48585.2020.9116510
32 Y. H. Chang, C. H. Chu, and H. W. Lin: Electronics **13** (2024) 882. https://doi.org/10.3390/electronics13050882
33 J. K. Lai, E. Merzari, and Y. A. Hassan: Int. J. Heat and Fluid Flow **75** (2019) 1. https://doi.org/10.1016/j.ijheatfluidflow.2018.11.002
34 F. P. Incropera: Fundamentals of heat and mass transfer (Wiley, 2006). https://dl.acm.org/doi/book/10.5555/1209497
35 I. Walter, I. Cidon, and A. Kolodny: IEEE Computer Arch. Letters **8** (2009) 5. https://doi.org/10.1109/L-CA.2008.11
36 A. S. Kim: Advanced Computational Fluid Dynamics for Emerging Engineering Processes (IntechOpen, 2018). https://doi.org/10.5772/intechopen.82266